

Optical Engineering

OpticalEngineering.SPIEDigitalLibrary.org

Long-range depth profiling of camouflaged targets using single-photon detection

Rachael Tobin
Abderrahim Halimi
Aongus McCarthy
Ximing Ren
Kenneth J. McEwan
Stephen McLaughlin
Gerald S. Buller

SPIE.

Rachael Tobin, Abderrahim Halimi, Aongus McCarthy, Ximing Ren, Kenneth J. McEwan, Stephen McLaughlin, Gerald S. Buller, "Long-range depth profiling of camouflaged targets using single-photon detection," *Opt. Eng.* **57**(3), 031303 (2017), doi: 10.1117/1.OE.57.3.031303.

Long-range depth profiling of camouflaged targets using single-photon detection

Rachael Tobin,^a Abderrahim Halimi,^a Aongus McCarthy,^a Ximing Ren,^a Kenneth J. McEwan,^b Stephen McLaughlin,^a and Gerald S. Buller^{a,*}

^aHeriot-Watt University, School of Engineering and Physical Sciences, Edinburgh, United Kingdom

^bDefence Science and Technology Laboratory, Porton Down, Salisbury, United Kingdom

Abstract. We investigate the reconstruction of depth and intensity profiles from data acquired using a custom-designed time-of-flight scanning transceiver based on the time-correlated single-photon counting technique. The system had an operational wavelength of 1550 nm and used a Peltier-cooled InGaAs/InP single-photon avalanche diode detector. Measurements were made of human figures, in plain view and obscured by camouflage netting, from a stand-off distance of 230 m in daylight using only submilliwatt average optical powers. These measurements were analyzed using a pixelwise cross correlation approach and compared to analysis using a bespoke algorithm designed for the restoration of multilayered three-dimensional light detection and ranging images. This algorithm is based on the optimization of a convex cost function composed of a data fidelity term and regularization terms, and the results obtained show that it achieves significant improvements in image quality for multidepth scenarios and for reduced acquisition times. © The Authors. Published by SPIE under a Creative Commons Attribution 3.0 Unported License. Distribution or reproduction of this work in whole or in part requires full attribution of the original publication, including its DOI. [DOI: [10.1117/1.OE.57.3.031303](https://doi.org/10.1117/1.OE.57.3.031303)]

Keywords: photon counting; three-dimensional image acquisition; light detection and ranging; low light level; image processing.
Paper 171571SS received Oct. 3, 2017; accepted for publication Dec. 1, 2017; published online Dec. 27, 2017.

1 Introduction

Light detection and ranging (LiDAR) continues to be the technique of choice in a variety of remote sensing applications.¹ The time-correlated single-photon counting (TCSPC) technique has more recently emerged as a candidate technology for LiDAR, due to its high sensitivity and excellent surface-to-surface resolution.² The TCSPC approach has been successfully demonstrated in a number of LiDAR applications, such as long-range depth imaging,^{3–5} underwater depth imaging,^{6,7} and multispectral depth imaging.⁸ The TCSPC technique was used to obtain both depth and intensity information for each pixel, building up a three-dimensional (3-D) image of the target scene by using scanning or multiple detector arrays.⁹ The use of high-sensitivity single-photon detectors, such as InGaAs/InP and Si single-photon avalanche diode (SPAD) detectors,^{10–12} means that low average optical power levels can be used even at long distances, resulting in the potential for low-power eye-safe imaging.

The identification of targets that have been obscured by clutter is a subject of significant relevance for long-range field applications, in particular. Several experiments involving “seeing” behind or through various obscuring media have been previously performed using LiDAR systems.^{13–17} References 13 and 14 present examples of 3-D laser radar imaging using a range-gated approach that can provide high-resolution gated images using very few laser pulses. This approach requires high energy laser pulses (typically μJ) and does not give a full surface profile of the target, but instead provides a range-gated intensity image. Henriksson et al.¹⁵ presented a scanning TCSPC system that was successful in

imaging targets through foliage at a distance of ~ 300 m. The slow scan speed of the system meant that in the example demonstrated the acquisition time was 30 min for a $5 \text{ deg} \times 1 \text{ deg}$ scene. Also, their algorithm for depth estimation did not take into account spatial correlations between neighboring pixels, resulting in many of the pixels providing no depth information due to a lack of returned photons. Some previous work has been performed on the image processing of targets behind obscuring surfaces and media, for example Refs. 16 and 17 described bespoke image processing algorithms designed for TCSPC data that reconstructed depth and intensity profiles. Wallace et al.¹⁶ presented an algorithm based on a reversible jump Markov chain Monte Carlo technique, which successfully reconstructed the depth profile of an object behind a wooden trellis fence at a stand-off distance of 325 m. While this approach works well and provides good depth information, the algorithm required significant processing times. The algorithm presented by Shin et al.¹⁷ was used to demonstrate high-resolution depth estimations for multiple surfaces with a low number of returned photons. The approach had relatively short processing times; however, the data were obtained in a laboratory-based trial at short target distances (around 4 m) and did not demonstrate the effects of high levels of ambient lighting or solar background.

In this paper, we explore the challenges of obtaining high-resolution depth images of objects obscured by camouflage netting using low laser powers at stand-off distances of hundreds of meters and in the presence of high ambient light levels. This paper also presents an advanced image processing algorithm specifically designed to reconstruct depth and intensity profiles of objects hidden in clutter or behind obscuring media. The new algorithm exploits spatial correlations in the photon data and was designed to be robust

*Address all correspondence to: Gerald S. Buller, E-mail: G.S.Buller@hw.ac.uk

was used to both focus the outgoing light on to the target and collect photons scattered back from the target. The collected return photons were routed to the receive channel and then coupled to the detector using a 10- μm -diameter core armored optical fiber. An electrically gated InGaAs/InP SPAD detector module (Micro Photon Devices) was used in these measurements, which had an operating wavelength range of 900 to 1700 nm and an active-area diameter of 25 μm . The detector was set with a 5-V excess bias and had a single-photon detection efficiency of $\sim 30\%$ at the operational wavelength.²² Due to the monostatic configuration of the system, the presence of backreflections from the optical components within the transceiver unit could result in problems resulting from saturation of the sensitive optical detection system. Hence, the detector was operated in an electrically gated-mode in synchronization with the pulsed laser return, with the detector gate positioned to avoid these spurious backreflections. For the measurements described in this paper, a 14-ns detector gate duration was used. Afterpulsing can also present difficulties when using InGaAs/InP SPAD detectors, causing increased background levels. Afterpulsing is caused by charge carriers being trapped in defects, which are subsequently released causing spurious avalanches.^{23,24} In order to reduce the deleterious effects of detector afterpulsing, a hold-off time was used to deactivate the detector for a predetermined duration after a recorded event, in order to allow the traps to empty without triggering further avalanches. In the measurements described in this paper a detector hold-off time of 40 μs was selected as a compromise between reducing the effects of afterpulsing and restricting the maximum count rate possible. More detailed descriptions of the electronic gating approach used for this detector are provided in Refs. 21 and 22. In order to reduce the effects of solar background, the receive channel was also spectrally filtered using a longpass filter (LP2) with a cut-on wavelength of 1500 nm, and a 10-nm FWHM bandpass filter (BP2), as shown in Fig. 1. The detector module provided the electrical stop signal for the TCSPC module, which was configured to output time-tagged detection events. The time-tagged event information was transferred to the control computer via a USB connection.

3 Estimation of Depth and Intensity Images using Cross Correlation

For each pixel, the time-tagged photons were used to construct timing histograms of the ToF information using 2 ps timing bins. Depth information was extracted from these histograms using a cross correlation method, described previously in Refs. 6 and 21. For each pixel, a cross correlation, c , was performed between an instrumental response, R , and the measured histogram, y

$$c_t = \sum_{i=1}^T y_{t+i} \times R_i, \quad (1)$$

where y_t is the timing histogram value at the t 'th bin and T is the total number of timing bins. The timing position corresponding to the highest peak in the cross correlation was calculated for each pixel to provide target depth information. For each pixel, the number of photons in a range of 200 timing bins around the centroid location was summed to obtain an estimate of the intensity (or reflectivity) of the

target. For these measurements, the instrumental response function R was obtained by performing a single-point measurement of a uniform, flat surface, which was placed in the same nominal plane as the target position. An example of the instrumental response function for the measurements presented in this paper is shown in Fig. 2. Contributions to the timing jitter originate from the detector response, laser pulse duration, and other electronic components such as the TCSPC module. In this case, the overall system jitter was 226 ps (FWHM), with the largest contribution being the detector jitter.

Typically, targets with a single reflecting surface will result in one peak per histogram, which corresponds to the target position (not including any peaks arising from backreflections as previously discussed). This means that pixelwise cross correlation can give satisfactory results since there is only one distinct target return (it is worth noting that the presence of background noise can affect the accuracy of these estimates). However, for targets behind camouflage netting or in obscuring media, the histograms may include

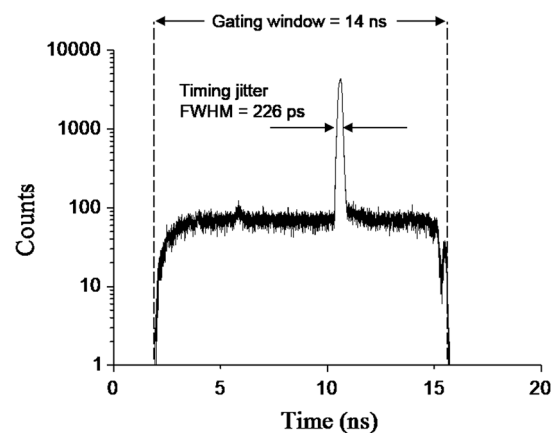


Fig. 2 Instrumental timing response taken from a uniform, scattering surface located in the same nominal plane as the target. The overall timing jitter (226 ps FWHM) of the system and the detector gating window of 14 ns duration are shown in the figure. An arbitrary zero was chosen for the displayed time-scale.

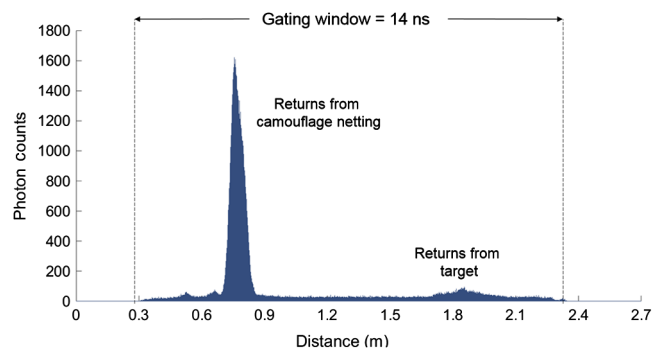


Fig. 3 Example of an aggregated timing histogram of a measurement of a target placed ~ 1 m behind camouflage netting. In this aggregated histogram, data from all 12800 pixels in the image are summed and displayed in this single histogram. In the figure, the larger peak consists of the returns from the camouflage netting and the smaller peak represents the returns from the target. The zero point in the depth axis is chosen arbitrarily, the camouflage netting was ~ 230 m from the transceiver.

multiple peaks, with the largest peak not necessarily corresponding to the target position. In this case, the cross correlation will assign a single depth point to only the largest return peak. To illustrate this, Fig. 3 shows an aggregated timing histogram constructed from an 80×160 pixel measurement of a target located at ~ 1 m behind a camouflage net. This particular histogram, shown in Fig. 3, is the sum of the histograms from all 12,800 pixels in the depth image. This figure clearly shows that the return from the camouflage netting is considerably greater than the return from the target placed behind the camouflage. Preliminary results show that more advanced image processing algorithms, designed for multisurface targets that exploit spatial correlations between neighboring pixels, can be used to reduce noise and improve image quality, as described in Sec. 5.

4 Depth Imaging Using the Cross Correlation Approach

A series of measurements were performed in daylight at a stand-off distance of 230 m from the transceiver unit. The weather was dry, with bright daylight and overcast cloud coverage, with conditions remaining stable for the duration of the measurements. This section presents preliminary results from these trials with depth and intensity estimation of targets obtained using the pixelwise cross correlation algorithm discussed in the previous section. The target scene comprised of an actor holding one item in different positions. The first set of measurements was performed with an unobstructed view of the actors and the second set was performed with a double layer of commercially available camouflage netting placed ~ 1 m in front of the actors' standing position (see Fig. 4).

The first set of targets was imaged at a stand-off distance of 230 m, unobscured by camouflage. The scanned area ($1 \text{ m} \times 2 \text{ m}$) was mapped by 80×160 pixels ($X \times Y$). This was equivalent to a pixel-to-pixel pitch of 12.5 mm in both X and Y at the target plane. The focused beam diameter at the target was ~ 1 cm, meaning that there was little or no overlap between adjacent pixels for each scan position. A per-pixel acquisition time of ~ 3.2 ms was used, which gave a total image scan time of 41.0 s. An average optical

power level of just less than 1 mW at the target was used at a laser repetition rate of 19.5 MHz. Figure 5 shows the results from two measurement scenarios: the first scenario consisted of an actor holding a rocket-propelled grenade (RPG) across his chest; the second scenario is a different actor holding a plank of wood in the same position. Both intensity and depth profiles were obtained using pixelwise cross correlation. In the results shown in Fig. 5, a threshold has been applied to the data to exclude pixels with very low levels of photon returns, since they were unlikely to originate from target returns. The corresponding pixels in the depth profile were subsequently excluded.

Due to the inherent problem of range ambiguity in high repetition rate ToF systems,²⁵ the depth range was taken from an arbitrary zero point. In a fixed repetition rate LiDAR system, range ambiguity occurs when there is more than one possible position for a reflecting surface, which occurs when, instantaneously, there is more than one optical pulse in transit. This maximum unambiguous distance (d_{rep}) is dependent on the fixed repetition rate (f_{rep}) of the laser as

$$d_{\text{rep}} = \frac{c}{2f_{\text{rep}}}, \quad (2)$$

where c is the speed of light in a vacuum. Given that a laser repetition rate of 19.5 MHz was used in these measurements, the maximum range for unambiguous determination of target distance was only ~ 7.7 m. Range ambiguity can be removed by a reduction in repetition rate—which can significantly increase measurement time—or by using techniques such as laser pulse trains composed of pseudorandom patterns or by the use of multiple sequential repetition rates.^{26,27} Some of the background noise exhibited around the target in Fig. 5 originates from photon returns from foliage far behind the target illuminated by earlier laser pulses. Differences in the material reflectivity and dimensions of both the RPG and the wooden plank are evident in the intensity and depth profiles, making the two objects easily discernible in this example. The number of photon returns is dependent on a variety of factors such as acquisition time, optical power level, and the reflectivity of the target material at the illumination wavelength.^{21,26,28} It is evident from these

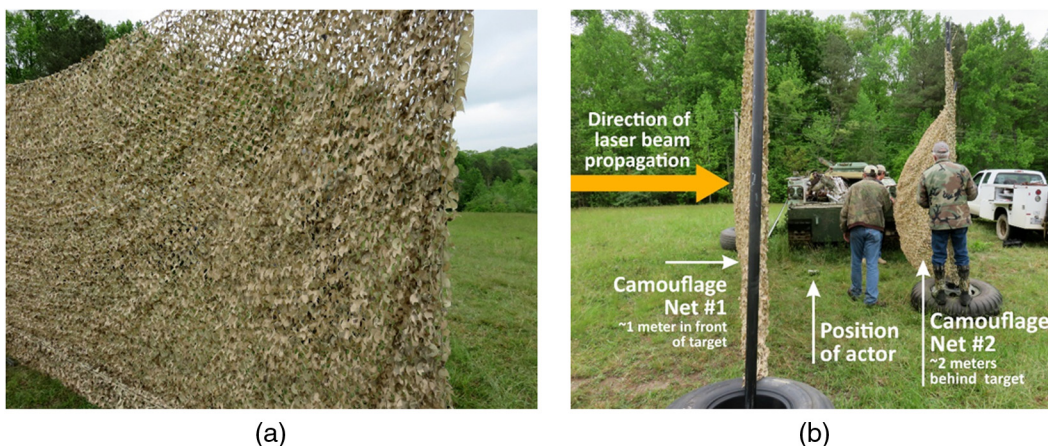


Fig. 4 (a) Front view photograph of the double layer of commercially available camouflage net which was located 1 m in front of the target position. (b) Side view of the setup showing both a double layer of camouflage in front of the target and a single layer behind the target.

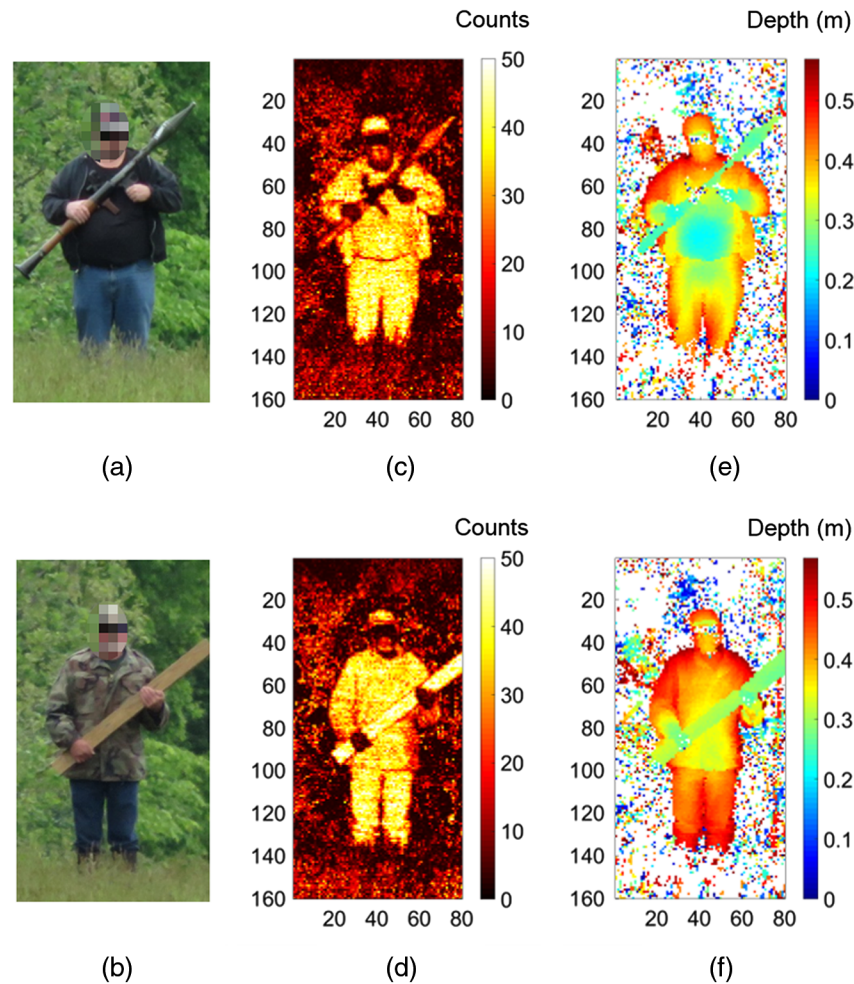


Fig. 5 Reconstructed depth and intensity measurements of two unobstructed targets: an actor holding an RPG across his chest and an actor with a wooden plank in the same position. These measurements were taken at a range of 230 m, with a per-pixel acquisition time of ~ 3.2 ms and an average optical power level of just under 1 mW. (a, b) Photographs of the two actors holding the RPG and a wooden plank, respectively. Both photographs were taken from the location of the transceiver unit using a Canon PowerShot SX700 HS digital camera with the zoom lens set to a focal length of 135 mm. In the photographs, the faces of the two actors were blurred for anonymity, although it should be noted that both actors are wearing dark eye-wear. (c, d) The intensity maps of both target scenes, with the color scale illustrating photon counts per pixel. (e, f) The depth profiles of both target scenes where the depth is shown on the color scale, with zero depth being close to the front surface of the target. A pixel format of 80×160 ($X \times Y$) is shown for each of the depth and intensity profiles.

images that at $\lambda = 1550$ nm, the clothes of the actors yielded a significant quantity of photon returns, whereas the gun handle and the actors' dark eye-wear yielded considerably less photon returns. Low photon returns from the face and hands demonstrate the low reflectivity of human skin at $\lambda = 1550$ nm, as previously shown in Ref. 29. In Fig. 5, the overall depth range of the image is ~ 0.5 m, and the depth profile appears to show subcentimeter depth features for most of the target.

The long acquisition time of the entire scan (41.0 s) used for these measurements was chosen in order to acquire an image with a far greater amount of photon returns than required. In these measurements, both the macrotime (time from start of scan) and the microtime (time between the corresponding start signal and the recorded photon arrival time) were recorded for each detection event. This meant that

we could use perpixel acquisition times that were shorter than the original measurement using shorter duration sections of each pixel's entire measurement data. The resulting depth profiles, for the scenario shown in Fig. 5(f), for per-pixel acquisition times of 3.2, 1.0, 0.5, and 0.1 ms, which correspond to image acquisition times of 41.0, 12.8, 6.4, and 1.3 s, respectively, are shown in Fig. 6.

As seen in Fig. 6, the quality of the depth profile degrades with decreasing acquisition time as the number of photons arriving back from the target decreases.

Using the same experimental parameters as used for the unobstructed scenarios, a series of measurements were performed with the target obscured by camouflage netting. The target scene consisted of an actor holding the object of interest (in this case a wooden plank held across the chest) ~ 1 m behind two layers of commercially available

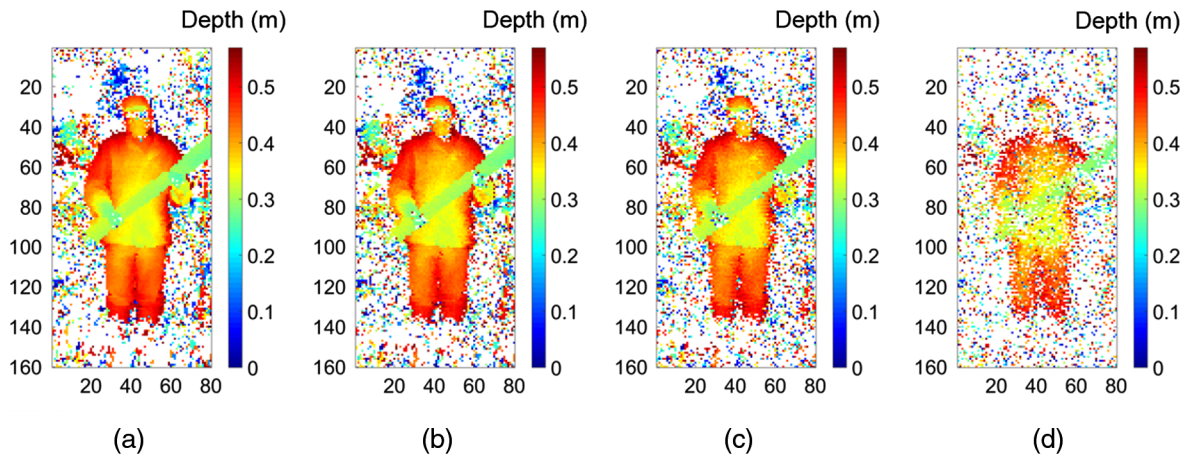


Fig. 6 Depth profiles of an unobstructed target (an actor with a wooden plank held across the chest) at a range of 230 m. The pixel format was 80×160 ($X \times Y$). Depth profiles were reconstructed from data with reduced acquisition time: (a) 3.2 ms per pixel, (b) 1.0 ms per pixel, (c) 0.5 ms per pixel, and (d) 0.1 ms per pixel.

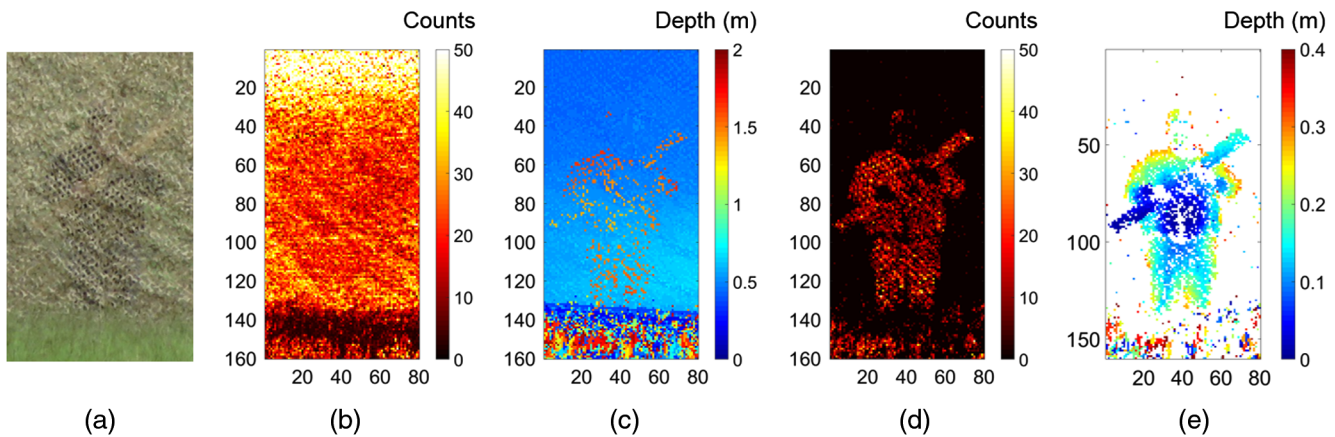


Fig. 7 Analysis of a scene with an actor holding a wooden plank across his chest and standing 1 m behind camouflage netting at an overall range of ~ 230 m. (a) A photograph of the actor holding the wooden plank behind the camouflage net. (b, c) The intensity and depth profiles of the target scene using the entire collected single-photon data. (d, e) The intensity and depth profiles after time gating to exclude all data except those within a 0.6 m range around the target location. The pixel format used in the depth and intensity profiles was 80×160 .

camouflage netting (see Fig. 4). Figure 7 shows the results of this scenario processed using the pixelwise cross correlation approach.

As can be seen in Fig. 7(b), when processed using pixelwise cross correlation, the intensity map only shows the camouflage netting due to significantly higher returns. Note that the netting moved slightly throughout the entire 41.0 s measurement duration due to a slight breeze. The depth map [Fig. 7(c)] shows a limited amount of detail from the obscured target where light has propagated through gaps in the camouflage net. In Fig. 7(c), the camouflage netting can be observed as being at the front of the depth profile (colored in blue) at a distance of 0.5 m from the reference point, whereas small regions of the target can be seen at a depth of ~ 1.5 m—a distance of 1 m behind the camouflage netting. Therefore, in order to more fully profile the target behind the camouflage, data were selected from only the 1900 timing bins, which correspond to a 0.6-m depth range centered around the target. The results [shown in

Figs. 7(d) and 7(e)] demonstrate that even behind a double layer of camouflage, our approach can provide depth and intensity reconstruction with approximately centimeter resolution. Such high quality depth and intensity profiling allow the targets to be identified in these examples. The “missing” pixels in the depth profile shown in Fig. 7(e) are where there were insufficient photon returns to provide depth estimations. In order to improve the quality of these depth and intensity images and permit use with low photon returns, a bespoke image processing algorithm was developed and will be described in the next section.

5 Restoration of Depth and Intensity Images Using an Algorithm Based on a Total Variation Approach

As highlighted in the results presented in Fig. 6, imaging a cluttered target (or reducing the acquisition time) can result in a large proportion of pixels to be either empty or contain

depth information from surfaces that are not relevant. This challenging problem has already been tackled by the image processing community and several algorithms, based on the Poissonian statistics of single-photon data, have been designed.^{15,17} For example, Shin et al.¹⁷ presented a reconstruction algorithm that restores multiple depths from an object behind a scattering media by solving a convex optimization problem accounting for the Poisson statistics and the sparsity of the data. However, this algorithm does not consider the possible spatial correlation of the hidden object and was only demonstrated using single-photon data obtained in indoor conditions over a range of 4 m. Alternatively, Henriksson et al.¹⁵ demonstrated a simple multisurface Gaussian fitting algorithm used in outdoor trials over tens of meters. This algorithm (i) filters the raw photon data to obtain a smaller number of peaks and (ii) uses a simple Gaussian fitting on the filtered histograms in order to obtain depth information.¹⁵ Again this approach does not account for the spatial correlations of the hidden object and may present poor results when the measurement time is reduced. In the presence of multiple surfaces and at low acquisition times, a reduced number of photon counts is collected, resulting in no depth data or highly erroneous depth information being assigned to a significant number of pixels using pixelwise-based approaches. The resulting data can be improved using image processing algorithms that take into account the spatial correlation of the observed targets.³⁰ In this paper, we consider a new algorithm that has two main objectives: (i) reducing the effect of Poisson noise affecting the observed histograms and (ii) reconstructing the different target surfaces. This is achieved by adopting a statistical approach that restores the LiDAR data while accounting for the Poisson data statistics and introducing prior information to improve the algorithm's performance. In this paper, we consider two prior assumptions, the first regularizes

intensities by accounting for spatial correlations between adjacent pixels; the second assumes a reduced number of detected peaks that are located in close depth regions, which regularizes the depths. By denoting by \mathbf{Y} the $(T \times N)$ observed histograms gathering the T bins and N pixels, the algorithm is based on the minimization of a cost function \mathcal{C} with respect to \mathbf{X} , as follows:

$$\mathcal{C}(\mathbf{X}) = \mathcal{L}(\mathbf{Y}, \mathbf{X}) + \tau_1 \phi_1(\mathbf{X}) + \tau_2 \phi_2(\mathbf{X}), \quad (3)$$

where $\tau_1 > 0$, $\tau_2 > 0$, and \mathbf{X} is a $(T \times N)$ matrix representing the cloud points after denoising and restoration of the observed targets. More precisely, the elements of the n 'th pixel $x_{t,n}$, $\forall t$ are zero except in the presence of a target at distance d_n , where the value $x_{d_n,n} = I_n$ will be associated with the target's intensity I_n . This cost function accounts for the Poisson statistics of the observed histograms (\mathbf{Y}) through the use of the log-likelihood of the data $\mathcal{L}(\mathbf{Y}, \mathbf{X})$. However, since the problem is ill-posed, additional information should be included to improve its results, which justifies the presence of the regularization terms ϕ_1 and ϕ_2 . The latter promote the following properties: (i) a small number of depths are active with respect to the observation range window; (ii) the observed objects present spatial correlations between adjacent pixels. Due to the fine depth resolution and the large observed range window, the first property assumes that the number of layers is lower than the number of available time bins, which is introduced using a collaborative sparse prior ϕ_1 associated with an L_{21} -mixed norm.³¹ The second property is promoted using a convex TV regularization term ϕ_2 , which is of great interest in the image processing community since it promotes smoothness while preserving edges. To deal with sparse data and because of the fine depth resolution, ϕ_2 assumes spatially correlated pixels after the sum of a predefined set of range bins.³²

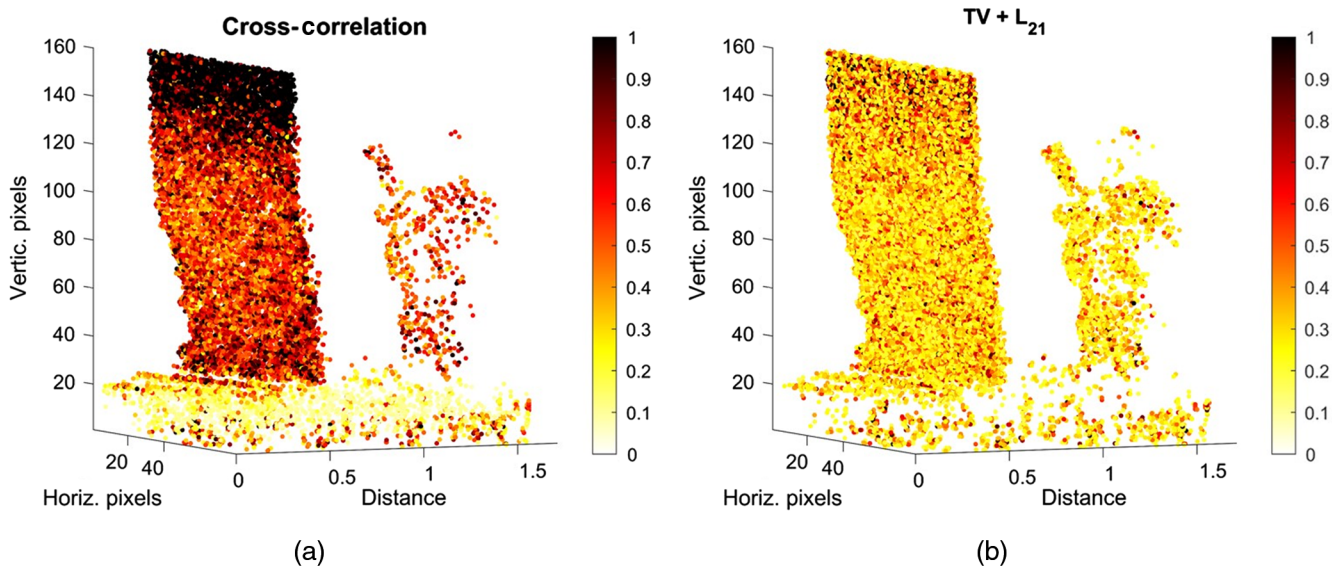


Fig. 8 Point cloud representation of the scene showing both depth and intensity. The target scene consisted of an actor holding a wooden plank when standing 1 m behind camouflage netting at a range of 230 m. The analysis was performed using (a) cross correlation and (b) the new TV + L_{21} algorithm. In both analyses (a) and (b), the entire histogram is analyzed in each case and no time gating was used. The zero point for the depth axis was chosen arbitrarily. The normalized intensities are represented by the color scale shown on the right of each image reconstruction.

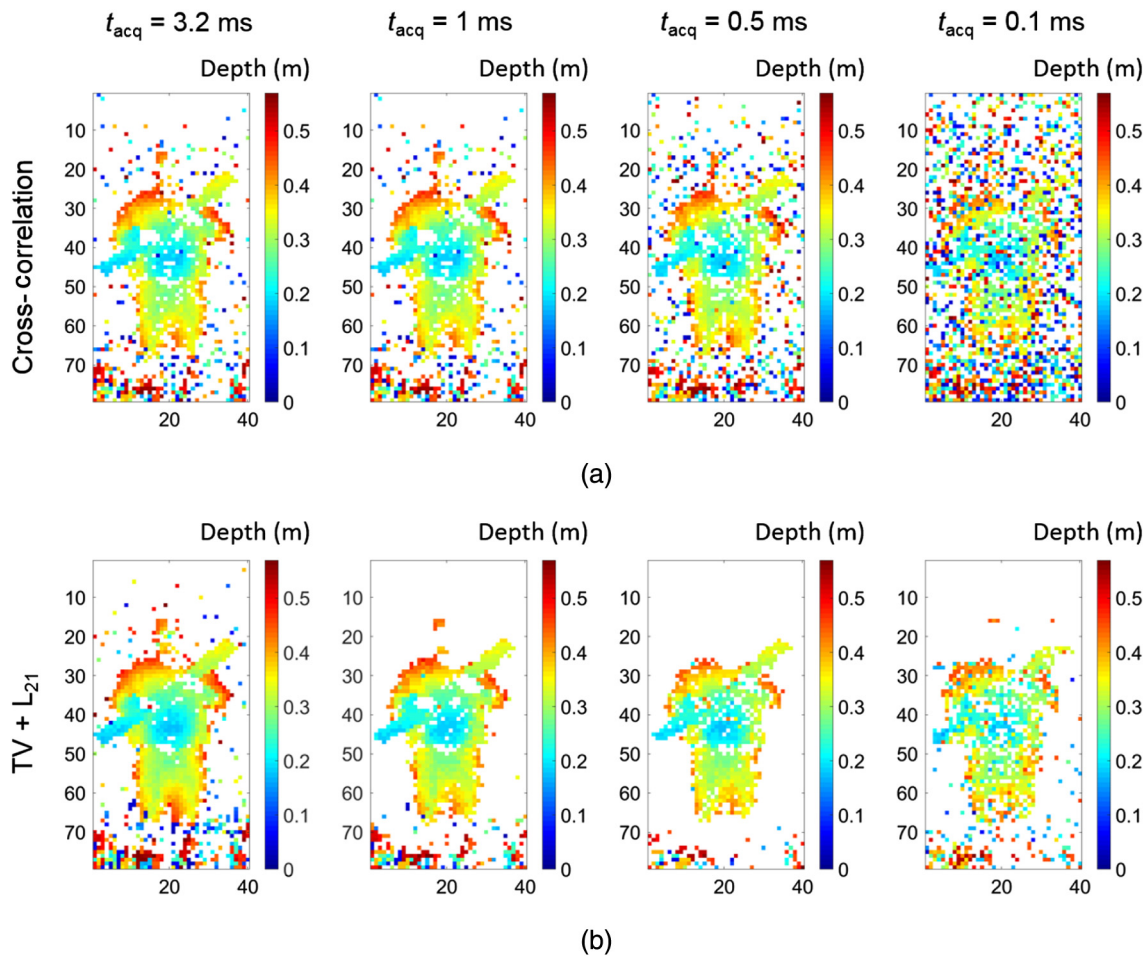


Fig. 9 Depth profiles of the target (actor holding a wooden plank) standing 1 m behind the camouflage netting. The depth reconstruction is for four different per-pixel acquisition times of 3.2, 1, 0.5, and 0.1 ms (shown left to right). (a) The pixelwise cross correlation algorithm used for time-gated data corresponding to 4 ns and (b) the new TV + L_{21} algorithm for the same time-gated data used in (a). This figure shows downsampled images of 40×80 pixels.

(a four neighborhood structure is considered with these results). The resulting algorithm is therefore denoted by TV + L_{21} to highlight the importance of these regularization terms. The cost function in Eq. (3) is convex and can be optimized using different convex algorithms, including the alternating direction method of multipliers algorithm considered in this paper.^{33,34} More details on the algorithm are presented in Ref. 35.

Figure 8 compares the pixelwise cross correlation with the TV + L_{21} approach when all the data are used, i.e., with no time gating of the data. The figure clearly shows that the TV + L_{21} algorithm has extracted more information from both the main reflecting surfaces, with the weaker signal from the target much more evident than in the case of cross correlation, which will only display the highest amplitude reflection in the histogram. The field trial data were then processed using the following steps: (i) filter the histograms using the TV + L_{21} algorithm (as in the case of the point cloud shown in Fig. 8), (ii) time gate the histograms to extract the temporal region of interest of the target, and (iii) determine the position and amplitude of the maximum of each pixel that correspond to the depth and intensity of the target. Figures 9 and 10 show the estimated depth and

intensity images obtained by the cross correlation and TV + L_{21} algorithms, for different acquisition times while considering downsampled images of 40×80 pixels from the 80×160 acquired pixels.

As expected, there is a decrease in the quality of the reconstructed image for both algorithms as the acquisition time is reduced, due to the photon returns being correspondingly lower. With reduced acquisition time, the cross correlation depth estimates exhibit a higher level of noise. However, the TV approach offers better restoration results where the noise surrounding the target is reduced, and the missing pixels of the part of the image comprising the human figure and the object of interest are restored. This performance was achieved as a result of considering the spatial correlation between pixels, and the use of collaborative sparsity to limit the number of active depths, which are mainly due to noise. A similar behavior is observed for the intensities where smoother and less noisy results are obtained by the image processing algorithm, especially at $t = 0.1$ ms, where the average photon return from the human target is well below one photon per pixel. These results highlight the interest of image processing algorithms in improving the performance of the sparsity-based single-photon data.

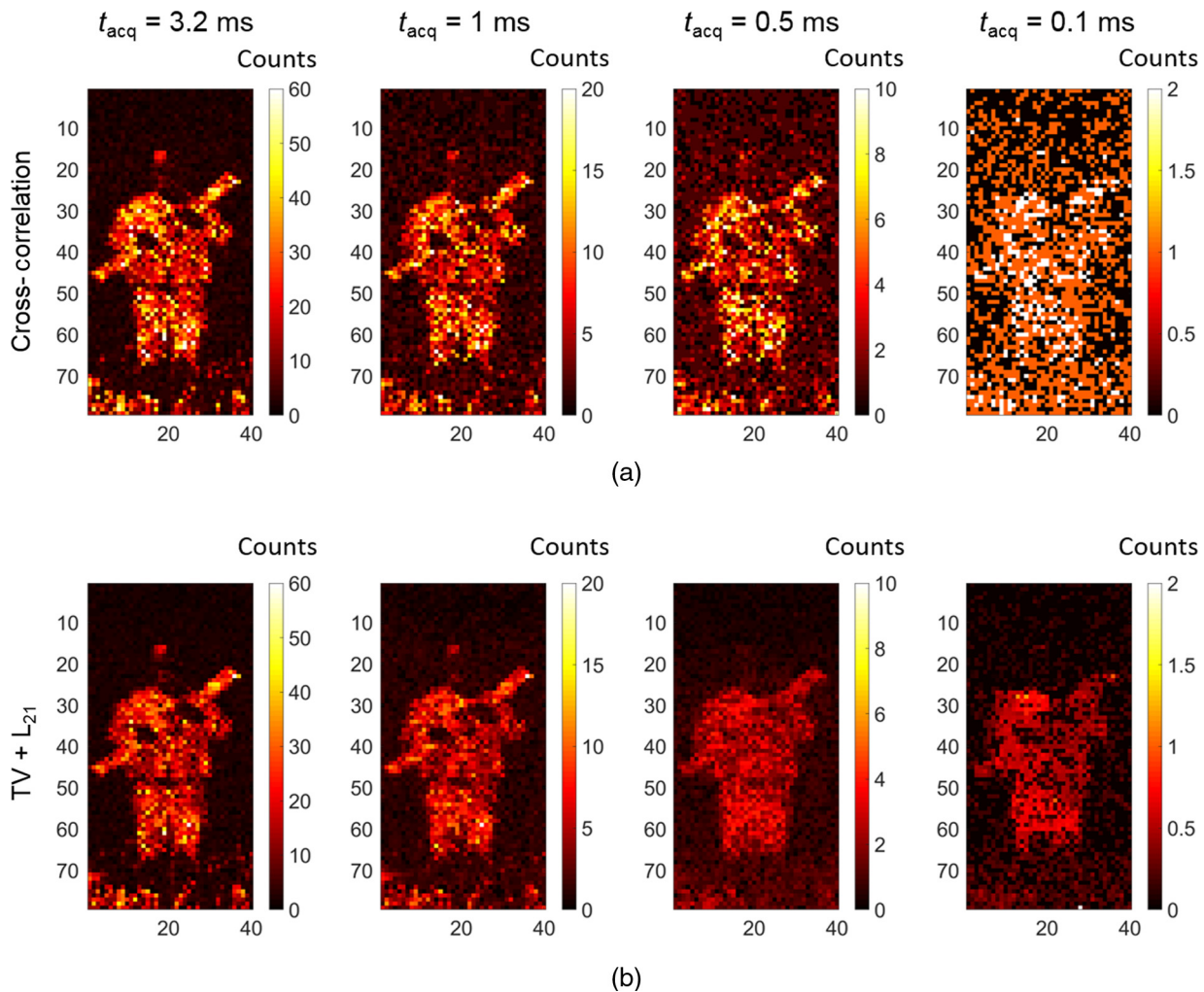


Fig. 10 Intensity profiles of the target (actor holding a wooden plank) standing 1 m behind the camouflage netting. The intensity reconstruction is for four different per-pixel acquisition times of 3.2, 1, 0.5, and 0.1 ms (shown left to right). (a) The pixelwise cross correlation algorithm used for time-gated data corresponding to 4 ns and (b) the new TV + L_{21} algorithm for the same time-gated data. This figure shows downsampled images of 40×80 pixels.

6 Conclusion

This paper presents reconstructions of high-resolution depth and intensity profiles of distant targets obscured by camouflage. The data used were acquired at outdoor field trials using a single-photon ToF scanner, and the images were reconstructed using extremely low levels of photon return, down to a level of under 1 photon per-pixel, on average. All measurements were taken at a stand-off distance of 230 m in daylight, and the scanning transceiver operated at a wavelength of 1550 nm. The pulsed laser used had an average optical power of just under 1 mW, although considerable reductions in measurement acquisition time are possible with a modest increase in laser power. Overall, a good level of target identification can be observed, even for the camouflaged targets. This paper also presented an algorithm to restore the 3-D data cube representing histograms of single-photon data. The proposed method is based on an optimization of a convex cost function composed of a data fidelity term and regularization terms. The proposed formulation and algorithm showed good restoration results when processing field trial data representing

a human figure standing behind a camouflage net. Such algorithm development and characterization will contribute to a more complete depth imaging model to inform next-generation single-photon transceiver design and to test the performance limits in terms of maximum stand-off distance, optical power requirements, and frame rate.

Acknowledgments

The authors thank Bradley Schilling of the US Army RDECOM CERDEC NVESD and his team for their assistance with the field trial measurements described in this paper. This work was supported by the Defence Science and Technology Laboratory (DSTL), the DSTL National PhD Scheme, and the UK Engineering and Physical Sciences Research Council Grants EP/N003446/1, EP/K015338/1, EP/M01326X/1, and EP/J015180/1.

References

1. V. Molebny et al., "Laser radar: historical perspective from the east to the west," *Opt. Eng.* **56**(3), 031220 (2017).
2. G. S. Buller and A. M. Wallace, "Ranging and three-dimensional imaging using time-correlated single-photon counting and point-by-point

- acquisition," *IEEE J. Sel. Top. Quantum Electron.* **13**(4), 1006–1015 (2007).
3. A. McCarthy et al., "Long-range time-of-flight scanning sensor based on high-speed time-correlated single-photon counting," *Appl. Opt.* **48**(32), 6241–6251 (2009).
 4. A. M. Pawlikowska et al., "Single-photon three-dimensional imaging at up to 10 kilometers range," *Opt. Express* **25**(10), 11919–11931 (2017).
 5. Z. Li et al., "Multi-beam single-photon-counting three-dimensional imaging lidar," *Opt. Express* **25**, 10189–10195 (2017).
 6. A. Maccarone et al., "Underwater depth imaging using time-correlated single-photon counting," *Opt. Express* **23**(26), 33911–33926 (2015).
 7. A. Halimi et al., "Object depth profile and reflectivity restoration from sparse single-photon data acquired in underwater environments," *IEEE Trans. Comput. Imaging* **3**, 472–484 (2017).
 8. A. M. Wallace et al., "Design and evaluation of multispectral lidar for the recovery of arboreal parameters," *IEEE Trans. Geosci. Remote Sens.* **52**(8), 4942–4954 (2014).
 9. D. Shin et al., "Photon-efficient imaging with a single-photon camera," *Nat. Commun.* **7**, 12046 (2016).
 10. R. H. Hadfield, "Single-photon detectors for optical quantum information applications," *Nat. Photonics* **3**(12), 696–705 (2009).
 11. S. Cova et al., "Avalanche photodiodes and quenching circuits for single-photon detection," *Appl. Opt.* **35**, 1956–1976 (1996).
 12. G. S. Buller and R. J. Collins, "Single-photon generation and detection," *Meas. Sci. Technol.* **21**(1), 012002 (2009).
 13. B. W. Schilling et al., "Multiple-return laser radar for three-dimensional imaging through obscurations," *Appl. Opt.* **41**(15), 2791–2799 (2002).
 14. O. Steinvall et al., "Performance of 3D laser radar through vegetation and camouflage," *Proc. SPIE* **5792**, 129–142 (2005).
 15. M. Henriksson et al., "Continuously scanning time-correlated single-photon-counting single-pixel 3-D lidar," *Opt. Eng.* **56**(3), 031204 (2017).
 16. A. M. Wallace et al., "Full waveform analysis for long-range 3D imaging laser radar," *EURASIP J. Adv. Signal Process.* **2010**(1), 896708 (2010).
 17. D. Shin et al., "Computational multi-depth single-photon imaging," *Opt. Express* **24**(3), 1873–1888 (2016).
 18. D. Killinger, "Free space optics for laser communication through the air," *Opt. Photonics News* **13**(10), 36–42 (2002).
 19. I. I. Kim, M. Mitchell, and E. J. Korevaar, "Measurement of scintillation for free-space laser communication at 785 nm and 1550 nm," *Proc. SPIE* **3850**, 49–62 (1999).
 20. F. Nadeem et al., "Continental fog attenuation empirical relationship from measured visibility data," *Radioengineering* **19**(4), 596–600 (2010).
 21. A. McCarthy et al., "Kilometer-range depth imaging at 1550 nm wavelength using an InGaAs/InP single-photon avalanche diode detector," *Opt. Express* **21**(19), 22098–22113 (2013).
 22. A. Tosi et al., "Fully programmable single-photon detection module for InGaAs/InP single-photon avalanche diodes with clean and sub-nanosecond gating transitions," *Rev. Sci. Instrum.* **83**(1), 013104 (2012).
 23. G. S. Buller et al., "Single-photon avalanche diode detectors for quantum key distribution," *IET Optoelectron.* **1**(6), 249–254 (2007).
 24. M. A. Itzler, X. Jiang, and M. Entwistle, "Power law temporal dependence of InGaAs/InP SPAD afterpulsing," *J. Mod. Opt.* **59**(17), 1472–1480 (2012).
 25. P. A. Hiskett et al., "A photon-counting time-of-flight ranging technique developed for the avoidance of range ambiguity at gigahertz clock rates," *Opt. Express* **16**, 13685–13698 (2008).
 26. N. J. Krichel, A. McCarthy, and G. S. Buller, "Resolving range ambiguity in a photon counting depth imager operating at kilometer distances," *Opt. Express* **18**(9), 9192–9206 (2010).
 27. Y. Liang et al., "1550 nm time-of-flight ranging system employing laser with multiple repetition rates for reducing the range ambiguity," *Opt. Express* **22**, 4662–4670 (2014).
 28. J. S. Massa et al., "Time-of-flight optical ranging system based on time-correlated single-photon counting," *Appl. Opt.* **37**(31), 7298–7304 (1998).
 29. C. C. Cooksey, B. K. Tsai, and D. W. Allen, "A collection and statistical analysis of skin reflectance signatures for inherent variability over the 250 nm to 2500 nm spectral range," *Proc. SPIE* **9082**, 908206 (2014).
 30. A. Kirmani et al., "First-photon imaging," *Science* **343**(6166), 58–61 (2014).
 31. P. Sprechmann et al., "Collaborative hierarchical sparse modeling," in *44th Annual Conf. on Information Sciences and Systems (CISS '10)*, pp. 1–6, IEEE (2010).
 32. L. I. Rudin, S. Osher, and E. Fatemi, "Nonlinear total variation based noise removal algorithms," *Phys. D* **60**(1), 259–268 (1992).
 33. S. Boyd et al., "Distributed optimization and statistical learning via the alternating direction method of multipliers," *FNT Mach. Learn.* **3**, 1–122 (2011).
 34. A. Halimi et al., "Fast hyperspectral unmixing in presence of nonlinearity or mismodeling effects," *IEEE Trans. Comput. Imaging* **3**, 146–159 (2017).
 35. A. Halimi et al., "Restoration of multilayered single-photon 3D lidar images," in *25th European Signal Processing Conf. (EUSIPCO '17)*, pp. 708–712 (2017).

Rachael Tobin is a PhD research student under the supervision of Professor Gerald S. Buller in the Institute of Photonics and Quantum Sciences at Heriot-Watt University. She received her B.Sc. (Hons) in physics from Heriot-Watt University and began her PhD in 2015. Her current research interests include single-photon LiDAR and imaging through obscurants at low light levels.

Abderrahim Halimi received his Eng. degree in electronics from the National Polytechnic School of Algiers, Algeria, in 2009, and both his MSc and PhD degrees in signal processing from the Institut National Polytechnique de Toulouse, Toulouse, France, in 2010 and 2013, respectively. From October 2013 to September 2015, he was a postdoctoral research associate with the University of Toulouse and the University of Technology of Troyes, France, under the support of the HYPANEMA ANR Project. Since November 2015, he has been a postdoctoral research associate within the School of Engineering and Physical Sciences, Heriot-Watt University. His research activities focus on statistical signal and image processing, with a particular interest in Bayesian inverse problems with applications to hyperspectral imaging, satellite altimetry, and single-photon depth imaging.

Aongus McCarthy received his BSc degree from the University College Galway, Galway, Ireland, in 1989, the diploma degree in electronics engineering from the Institute of Technology, Carlow, Ireland, in 1990, his BSc degree in physical optoelectronics from Essex University, Essex, United Kingdom, in 1991, and his PhD in physics from Heriot-Watt University, Edinburgh, United Kingdom, in 2002. He worked in industry from 1992 until 1997 as a design team leader on the development of a thermal transfer printing system. He is currently a research fellow with the School of Engineering and Physical Sciences, Heriot-Watt University. His research interests include optical and optomechanical system design, time-of-flight depth imaging, single-photon counting technologies, and microscope systems. He is a member of the Optical Society of America (OSA) and the IEEE Photonics Society.

Ximing Ren received his PhD in physics with a prize scholarship from the Scottish Universities Physics Alliance in the Single-Photon Group at Heriot-Watt University, United Kingdom, studying single-photon time-of-flight imaging under the supervision of Prof. Gerald S. Buller in 2015. He is currently a postdoctoral research associate with the Institute of Photonics and Quantum Sciences, Heriot-Watt University. He is interested in the research of sparse photon depth imaging, using single-photon detectors. This involves optical imaging at the extreme levels of sensitivity and time resolution in order to reconstruct 3-D profiles of objects in challenging environments (e.g., underwater or at long distances). He is a member of the OSA.

Kenneth J. McEwan graduated with a BSc (Hons) degree in physics from the University of Strathclyde in 1986 then joined the Royal Signals and Radar Establishment (RSRE) in Malvern. While working at RSRE he obtained a DPhil degree in physical chemistry from the University of Oxford in 1991. He is currently a fellow at the Defence Science and Technology Laboratory at Porton Down and a fellow of the UK Institute of Physics. His role covers the military applications of electro-optic systems with current interests in advanced thermal imaging, imaging through obscurations, and stand-off chemical detection.

Stephen McLaughlin is a professor of signal processing and head of the School of Engineering and Physical Sciences. His research interests lie in the fields of adaptive signal processing and nonlinear dynamical systems theory and their applications to biomedical, energy and communication systems. He is a fellow of the Royal Academy of Engineering, the Royal Society of Edinburgh, the Institute of Engineering and Technology, and the IEEE.

Gerald S. Buller graduated with his BSc (Hons) degree in natural philosophy from the University of Glasgow in 1986 and his PhD in physics from Heriot-Watt University in 1989. Currently, he is a professor of physics at Heriot-Watt University and holds an EPSRC established career fellowship. He cofounded Helia Photonics Ltd. in 2002, where he remains company chairman. He is a fellow of the Royal Society of Edinburgh, a fellow of the UK Institute of Physics, and a fellow of the OSA. His research interests are single-photon physics and applications, including single-photon imaging, single-photon detectors, and quantum communication.